Organic Electronics 70 (2019) 219–226

Contents lists available at ScienceDirect

Organic Electronics

journal homepage: www.elsevier.com/locate/orgel

Influence of the bias-dependent emission zone on exciton quenching and OLED efficiency

Markus Regnat[a,b,*], Kurt P. Pernstich[a], Beat Ruhstaller[a,c]

[a] Zurich University of Applied Sciences ZHAW, Institute of Computational Physics, Technikumstrasse 9, 8401, Winterthur, Switzerland
[b] Institut des Matériaux, Ecole Polytechnique Fédérale de Lausanne, EPFL, Station 12, 1015, Lausanne, Switzerland
[c] FLUXIM AG, Technoparkstrasse 2, 8406, Winterthur, Switzerland

ARTICLE INFO

Keywords:
OLED
Electro-optical device model
Emission zone shift
Light outcoupling factor
Exciton quenching
Efficiency roll-off

ABSTRACT

We present an electro-optical model of a three-layer phosphorescent OLED which accurately describes the measured current efficiency and transient electroluminescence decay for different biases. Central findings are a bias-dependent emission zone, which influences light outcoupling as well as exciton quenching, and the presence of strong triplet-polaron quenching even at low bias. The measured current efficiency initially increases up to 9 V before it decreases, where the increase is found to be caused by reduced triplet-polaron quenching with holes, while the decrease is caused by a reduced light outcoupling and increased triplet-triplet annihilation. The numerical model allows identifying the individual contributions of the exciton continuity equation and explains the electroluminescence decay, which deviates significantly from a mono-exponential decay due to the dominating influence of exciton generation and quenching after the external bias is removed.

1. Introduction

Over the last years OLED efficiencies increased up to nearly 40% due to the use of orientated phosphorescent [1–4] and TADF emitters [5–8] with internal quantum efficiencies close to 100%. Including different light scattering strategies for improved light outcoupling from the OLED stack, remarkable EQEs up to 62% were achieved [9–11]. Besides reaching high efficiencies, a major challenge for realizing OLEDs with high luminous intensities is still the efficiency roll-off at high biases due to exciton quenching processes, namely triplet-polaron quenching (TPQ) and/or triplet-triplet annihilation (TTA) [12,13].

To improve further the light emission at high biases, a better understanding of the underlying mechanisms, especially at high biases, is necessary. An important OLED characterization parameter is the current efficiency (CE) [14–16], which gives the ratio of the photometric measure luminance L to the applied current density j.

$$CE = \frac{L}{j} \quad (1)$$

In this study, we show that a bias-dependent position of the emission zone has an influence on the CE, as well as on the electroluminescence (EL) decay. Direct experimental evidence of a bias-dependent emission zone in the investigated OLED from optical measurements was presented by us recently [17]. In the work presented here, an elaborate electro-optical model is parametrized to describe quantitatively the measured current-voltage-luminance, the current efficiency, and the transient electroluminescent decay. This model also shows a strong bias dependence of the emission zone and further reveals that significant exciton quenching occurs already at low bias and that the strength of exciton quenching is influenced by the bias-dependent emission zone. Only with a combination of a bias-dependent emission zone - which influences the light outcoupling as well as exciton quenching - the observed trends in CE and EL decay can be explained.

Our study sheds light on the interplay between the position of the emission zone and exciton quenching, and highlights the importance of considering the details of the emission zone, particularly a possible bias dependence, when optimizing OLED efficiency.

2. Experimental

2.1. OLED fabrication

The investigated phosphorescent OLED stack (see inset to Fig. 1) consists of indium tin oxide ITO (100 nm)/PEDOT:PSS (30 nm)/TCTA (46 nm)/CBP:Ir(ppy)2(acac) (35 nm, 5 wt%)/NBPhen (52 nm)/Ca (15 nm)/Al (100 nm). The organic materials poly(3,4-ethylenedioxythiophene):polystyrene sulfonate (PEDOT:PSS), 4,4′,4″-tris(carbazol-

* Corresponding author. Zurich University of Applied Sciences ZHAW, Institute of Computational Physics, Technikumstrasse 9, 8401, Winterthur, Switzerland
E-mail address: markus.regnat@zhaw.ch (M. Regnat).

https://doi.org/10.1016/j.orgel.2019.04.027
Received 31 January 2019; Received in revised form 12 April 2019; Accepted 17 April 2019
Available online 23 April 2019

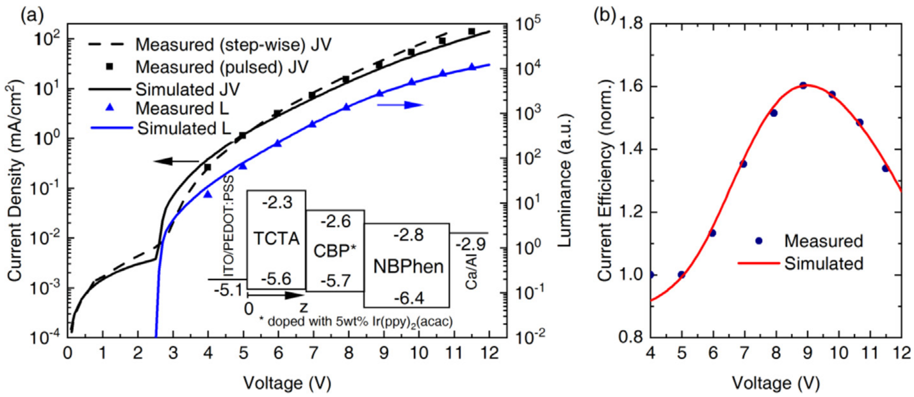

Fig. 1. Measured and simulated current density - voltage - luminance characteristic (a) and measured and simulated current efficiency for increasing bias (b) of the investigated OLED. The inset in (a) shows the OLED layer stack.

9-yl) triphenylamine (TCTA), 4,4′-bis(carbazol-9-yl)biphenyl (CBP), bis(2-phenylpyridine)(acetylacetonate)iridium(III) ($Ir(ppy)_2(acac)$) and 2,9-bis(naphthalen-2-yl)-4,7-diphenyl-1,10-phenanthroline (NBPhen) were purchased from Heraeus Clevios™ and Lumtec. The glass substrates with patterned ITO anode were purchased from Ossila Ltd. The substrates were cleaned with acetone and isopropanol in an ultrasonic bath and afterwards for 15 min with UV-ozone. A 30 nm thick PEDOT:PSS film was spin coated in air and subsequently heated in a glovebox for 40 min at 150 °C. All organic layers were deposited in high vacuum ($< 10^{-6}$ mbar) by thermal sublimation. For the emission layer $Ir(ppy)_2(acac)$ and CBP were co-evaporated. Prior to the cathode deposition, the shadow masks were exchanged under nitrogen atmosphere to obtain a pixel area of 4.5 mm^2. After film deposition, the OLEDs were encapsulated under nitrogen atmosphere.

2.2. Measurements

The electro-optical measurements were performed with the all-in-one measurement system Paios and the characterization suite 4.12 from Fluxim [18]. To measure the luminance a gated photomultiplier tube (PMT H11526 Series) from Hamamatsu was employed and controlled with Paios. The PMT output voltage V_{PMT} is directly proportional to the luminance because the electroluminescence (EL) spectrum is bias-independent, thus the PMT signal can be easily converted into luminance with the luminous sensitivity of the PMT. The acceptance angle of the PMT was $\approx \pm 10°$, and the measured luminance is proportional to the luminance at 0° to the surface normal (as obtained from the simulations) because the angular emission spectrum is essentially independent of the bias. To measure the J-V-L characteristics, voltage pulses with magnitudes from 4 to 12 V were applied to the OLED while measuring the current density j and the luminance L. The length of the voltage pulses was set to 200 μs in order to reach steady state, and the values for j and L were averaged over the last 20 μs of each pulse. For the transient EL decay measurements the on-voltage was applied for 200 μs before turning-off the OLED by applying 0 V. The JV characteristics was also measured using a higher precision, stepwise voltage ramp with longer integration time to obtain the J-V curve over the entire bias range.

2.3. Electro-optical model

Electro-optical simulations were carried out with a preview version of Setfos 5.0 (Fluxim) [19]. Setfos calculates the position- and time-dependent charge carrier density distribution, exciton generation, diffusion and decay, and outcoupling of photons [20,21]. In the electro-optical model, the exciton generation occurs via Langevin recombination inside the emission layer (EML), and exciton diffusion is limited to the EML. Generation of photons from radiatively decaying excitons considers the Purcell effect [21,22]. Mode analysis was used to divide the generated photons into photons that are absorbed, emitted and dissipated in evanescent, substrate and guided mode [21]. Mode analysis in Setfos considers emission either into the entire hemisphere or into a restricted angular range. An angular range of ± 10° was used to be able to compare the emitted photons with the measured luminance. To explain the measurements, we had to include multiple exciton quenching mechanisms in the model, namely triplet-polaron quenching for holes (TPQh) and for electrons (TPQe) as well as triplet-triplet annihilation (TTA). All model parameters are listed in table A1.

2.4. Optimization of the model parameters

A pattern search optimization algorithm with a genetic search routine implemented in Matlab was used to optimize the model parameters to obtain a good agreement between simulations and measurements. In each iteration, the optimizer started Setfos to calculate the electro-optical characteristics (current density - voltage (J-V), current efficiency (CE) and transient electroluminescence (EL)), which were used to calculate the goodness of fit. The initial values and reasonable bounds for the model parameters were taken or estimated from literature [23–31]. Out of the 35 model parameters, 20 were allowed to vary (see table A1).

Despite the large number of free model parameters, we estimate that the obtained solution is close to a global optimum, because many of the parameter clusters influence only a certain subset of the dataset and, thus, they cannot be changed independently. While the simultaneous use of three different measurement types (J-V-L, CE, transient EL) in the fit prolongs the optimization process, they help, at the same time, to arrive closer to a global solution. As was demonstrated in an earlier study [32], the use of datasets from multiple measurement types is advised as it reduces the correlation among the model parameters.

3. Result and discussion

Fiugre 1a shows the measured and simulated current density and luminance for different applied biases. The J-V curve was measured in pulsed and stepwise mode as described in the experimental section. The step-wise measured JV curve shows a slightly higher current at high voltages than the pulsed measurement, possibly due to self-heating [33]. The measured and simulated values agree very well, indicating the high quality of the model, and the inset to Fig. 1a shows the layer stack of the phosphorescent OLED. Fig. 1b shows the measured and simulated current efficiency (CE).

The large increase of the current efficiency between 5 V and 9 V is somewhat unexpected and can only be explained by considering a bias-dependent change of the emission zone and its influence on the exciton quenching contributions, as discussed in detail below. An increase in CE and EQE has been reported before [35–37] and was explained by a non-constant charge balance [34], which agrees with the findings presented here. The decreasing CE at large bias can only be explained by considering exciton quenching as well as the bias-dependent change of the emission zone, which leads to a reduced light outcoupling at high bias as discussed next.

3.1. Influence of the emission zone on light outcoupling

In the electro-optical model, the luminance at 0° to the surface normal is calculated from Ref. [38]:

$$L = 683\,\frac{lm}{W}\cdot\int \bar{y}(\lambda)\cdot\frac{1}{2\pi}\cdot E_\gamma(\lambda)\cdot\Lambda(\lambda)\cdot\int N_\gamma(z)\cdot g(z,\ \lambda)dz\,d\lambda. \tag{2}$$

The value of 683 lm/W is the maximum of the luminous efficacy, $\bar{y}(\lambda)$ is the dimensionless photopic luminosity function, $E_\gamma(\lambda)$ is the photon energy, and $\Lambda(\lambda)$ the intrinsic luminescence spectrum of the emitting species. $N_\gamma(z)$ is the position-dependent number of photons generated from the emitting dipoles, and $g(z,\ \lambda)$ accounts for the optical feedback of the OLED micro cavity on the emitting dipoles including the effects of evanescent and guided modes, interference, light trapping due to total internal reflection as well as absorption in the individual layers [38].

To describe the influence of the bias-dependent emission zone on light outcoupling, we introduce the light outcoupling factor $\xi(z)$ shown in Fig. 2, which quantifies the emitted luminance at 0° to the surface normal as a function of emitter position. To obtain $\xi(z)$, the luminance was calculated as a function of the position z of a single emissive dipole and normalized to its maximum value. The light outcoupling factor has a maximum close to the EML/ETL interface. The maximum is slightly shifted towards the hole transport layer (HTL) because the evaporated electron transport layer (ETL) thickness was slightly lower (52 nm) than the optimum value (56 nm) obtained from simulations performed prior to device fabrication. At the HTL/EML interface, $\xi(z)$ is reduced by almost 50% due to a reduction of $g(z)$.

In addition, Fig. 2 shows the spatial distribution of the generated photons $N_\gamma(z)$ for different biases (dashed lines). At low biases, photons are mainly generated at the EML/ETL interface, while for higher biases, the maximum of the emission originates from the HTL/EML interface. The solid lines in Fig. 2 represent the influence of the light outcoupling on the generated photons. Integrating the effect of the position-dependent light outcoupling factor and the bias-dependent distribution of generated photons over the entire EML results in a 3% reduction of emitted photons at low bias and in a 25% reduction at high bias as indicated with the shaded areas in Fig. 2.

These outcoupling losses caused by the shifting emission zone reduce the luminance and contribute significantly to the reduction of the CE at high biases (cf. equation (1)). However, to describe the initial increase of CE, exciton quenching has to be considered as discussed in the following.

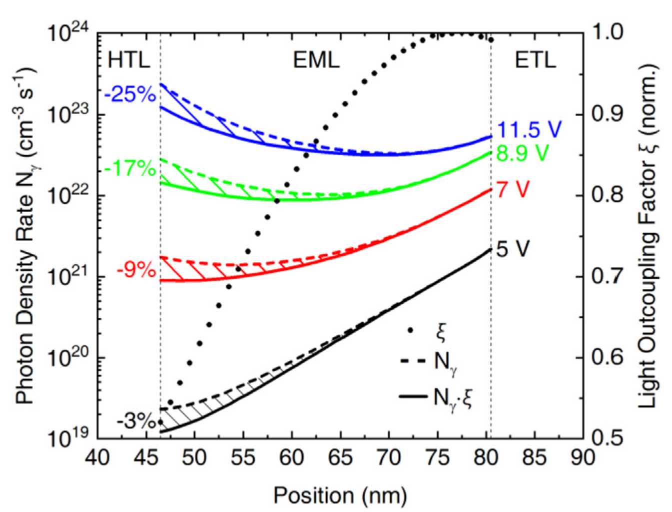

Fig. 2. Bias-dependent spatial distribution of generated photons before (dashed lines) and after (solid lines) considering the influence of the position-dependent light outcoupling factor (dotted line). The shift of the main emission from the EML/ETL interface to the HTL/EML interface reduces the emitted photons (shaded area) due to a lower light outcoupling factor $\xi(z)$.

3.2. Influence of the emission zone on exciton quenching

As discussed above, the spatial distribution of emitting dipoles is strongly bias-dependent, which also influences the exciton quenching contributions at different biases. In the electro-optical model, the exciton physics is modeled with the following exciton continuity equation:

$$\begin{aligned}\frac{d\mathscr{T}(t,z)}{dt} &= G\cdot R(t,z) + \nabla J_s(t,z) - F(z)\cdot k_{rad}\cdot\mathscr{T}(t,z) - k_{nonrad}\\ &\quad\cdot\mathscr{T}(t,z) - k_{TPQh}\cdot\mathscr{T}(t,z)\cdot p(t,z) - k_{TPQe}\cdot\mathscr{T}(t,z)\\ &\quad\cdot n(t,z) - \ k_{ann}\cdot\mathscr{T}(t,z)^2\end{aligned} \tag{3}$$

$G\cdot R(t,z)$ is the generation term for the time- (t) and position- (z) dependent triplet exciton density $\mathscr{T}(t,z)$, which is calculated from the exciton formation ratio $G = 1$ and the Langevin recombination rate R, where R is proportional to the electron and hole density in the EML ($R \propto n(t,z)\cdot p(t,z)$) [20]. Only the triplet exciton equation is relevant because any singlet excitons quickly relax to triplet states on the Ir $(ppy)_2$(acac) emitter as no host emission and no fluorescence emission from the emitter was observed. $\nabla J_s(t,z) \propto \frac{d^2T}{dx^2}$ is the exciton diffusion term, and $F(z)\cdot k_{rad}\cdot\mathscr{T}(t,z)$ describes radiative recombination of excitons with a rate constant k_{rad} modified by the position-dependent Purcell factor $F(z)$. The term $k_{nonrad}\cdot\mathscr{T}(t,z)$ represents non-radiative recombination with a rate constant k_{nonrad}. The terms $k_{TPQh}\cdot\mathscr{T}(t,z)\cdot p(t,z)$ and $k_{TPQe}\cdot\mathscr{T}(t,z)\cdot n(t,z)$ are the position-dependent triplet-polaron quenching terms, depending on the hole- and electron density with k_{TPQh} and k_{TPQe} being the respective rate constants. $k_{ann}\cdot\mathscr{T}(t,z)^2$ is the position-dependent triplet-triplet annihilation term with a rate constant k_{ann}. Integrating the terms in equation (3) over the emission layer yields the total contributions of each mechanism to the exciton continuity equation.

Fig. 3 shows the bias dependence of the individual terms at steady state ($\frac{d\mathscr{T}(t,z)}{dt} = 0$). Exciton generation (black line) increases with bias as expected. The main contribution reducing the number of excitons is

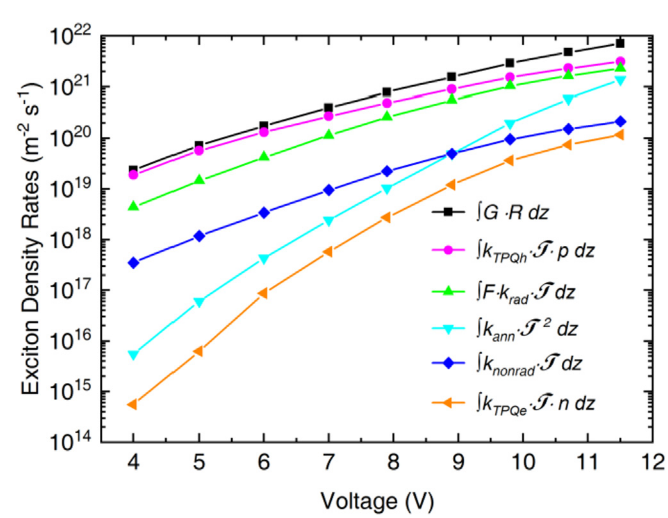

Fig. 3. Integrated terms of the exciton continuity equation for different biases. The integrated diffusion term is zero.

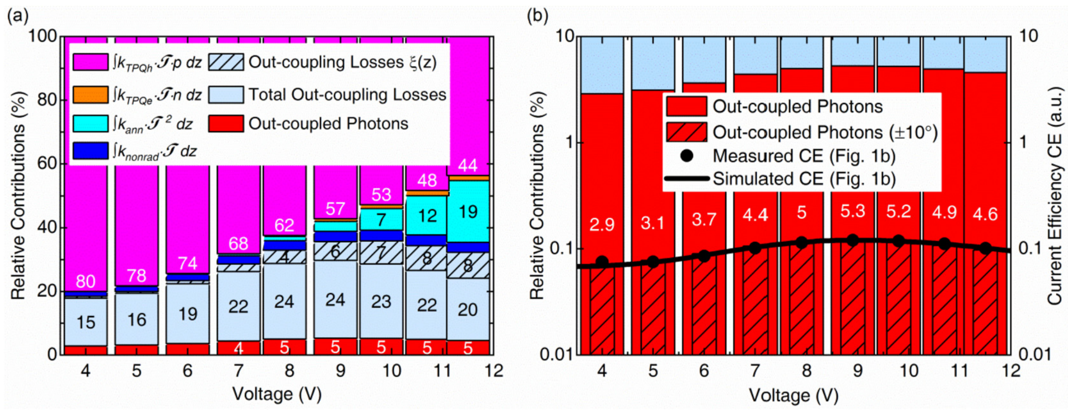

Fig. 4. Relative contributions of the individual terms of the exciton continuity equation where 100% corresponds to the total number of generated excitons (a) and the comparison of the outcoupled photons to the measured and simulated current efficiency (b). See text for details.

triplet-polaron quenching with holes (magenta line), followed by radiative recombination (green line). Triplet-triplet annihilation (cyan line) is strongly bias-dependent and becomes increasingly important at high bias. Non-radiative recombination (blue line) and triplet-polaron quenching with electrons (orange line) are only minor contributions to the exciton balance, which agrees with findings in Adachi et al. [23] and Oyama et al. [28]. The diffusion term in equation (3) vanishes after integration because exciton diffusion is limited to the EML.

Fig. 4a shows the relative contribution of the individual terms of the exciton continuity equation (eq. (3)) at each bias where 100% corresponds to the total number of generated excitons. The photons emitted into the hemisphere (red bars) are calculated via mode analysis from the radiatively decaying excitons ($\int F(z)\cdot k_{rad}\cdot\mathscr{T}(t,z)dz$). The light blue bars indicate the photons lost in evanescent, substrate and guided modes and through absorption. Fig. A1 shows these individual contributions. The shaded area in the light blue bars in Fig. 4a indicate the lost photons due to the light outcoupling losses described by $\xi(z)$. As discussed in the context of Fig. 2, the position-dependent light outcoupling factor $\xi(z)$ and the bias-dependent distribution of generated photons leads to a reduction of emitted photons by up to 25% for increasing biases. This corresponds to a loss of up to 8% of the generated excitons (shaded area in Fig. 4a). At low biases, the outcoupling losses due to EMZ change contribute with less than 1%.

Fig. 4b zooms into the region of out-coupled photons in Fig. 4a, and shows the percentage of photons emitted into an angular range of $\pm$ 10° (shaded bars) which increases up to 9 V before it decreases again at higher biases. The ratio of these out-coupled photons to generated excitons exactly resembles the measured current efficiency (cf. Fig. 1b), because the CE can also be calculated from the ratio of emitted photons ($\propto L$) and generated excitons ($\propto J$).

The contributions of non-radiative recombination (blue bars in Fig. 4a) and triplet-polaron quenching with electrons (orange bars in Fig. 4a) are essentially bias-independent and contribute with 1–2% and 1–3% to the total losses of generated excitons. Triplet-triplet annihilation (cyan bars in Fig. 4a) becomes significant at high bias due to the quadratic dependence on exciton density and contributes up to 19% to the total losses. As can be seen from the magenta bars in Fig. 4, triplet-polaron quenching with holes is the largest loss mechanism. Interestingly, the TPQh losses at low bias are rather large and decrease at higher bias. The behavior of TPQ with holes is explained in Fig. 5, which shows the exciton distribution together with the electron and hole densities for 5 and 11.5 V.

At 5 V (Fig. 5a) the majority of electrons are in the ETL, while the holes accumulate at the EML side of the EML/ETL interface. Thus, the exciton density has a maximum at this interface and TPQ with holes is prominent. At 11.5 V (Fig. 5b), a significant amount of electrons is being injected into the EML. Due to the larger field-dependence of the mobility for electrons than for holes, the effective electron mobility is larger than the hole mobility (cf. insets to Fig. 5), electrons accumulate at the HTL/EML interface. The main exciton density is now at the HTL/EML interface where the hole density is low, and TPQ with holes becomes less prominent at high biases. We like to note that the large field dependent electron mobility is required to explain the shift of the EMZ with bias as presented previously [17].

In References [39,40], two similar OLED stacks with larger EQE and similar emission zone have been presented. In those OLEDs, no energy barrier for electrons was present at the EML/ETL interface. When zeroing this energy barrier in our model, an increased electron density in the EML close to the EML/ETL interface is obtained. These electrons recombine, thereby reducing the number of excessive holes present at the EML/ETL interface. This significantly reduces the contribution of TPQ to 9% and increases the EQE to 13%. The EQE is, thus, strongly influenced by this energy barrier.

From the insights gained from the electro-optical model, the measured current efficiency (cf. Figs. 1 and 4a and b) can be well understood: The initial CE increase is due to a reduction of TPQ with holes because the emission zone shifts away from regions with large hole density. The decrease of CE at high bias is caused by increased TTA losses and by increased outcoupling losses due to the shifting emission zone. Thus, both CE trends, the increase and the decrease, are linked to the bias-dependent emission zone.

3.3. Influence of the emission zone on the EL decay

The decay time of emissive dipoles is known to depend on the local optical environment, and can be described by considering the position-dependent Purcell factor $F(z)$. The Purcell effect describes the dynamics of the dipole emission within an optical cavity, and a lower Purcell factor leads to a reduced spontaneous emission rate, and, thus, to a longer decay time [20]. Because the emission zone in the investigated OLED stack shifts with bias, the electroluminescence decay rate is expected to change due to the Purcell effect. Fig. 6 shows the position-dependent Purcell factor together with the radiative exciton density rate calculated with the true Purcell factor (solid lines) and with a fictitious, constant Purcell factor of 1.65 (dashed lines). At low bias, the main emission originates at the EML/ETL interface with F being 1.65, while for high biases, the emission zone shifts towards the HTL/EML interface where F is reduced to 1.2.

The shaded area in Fig. 6 indicates the reduction of the radiative exciton decay rate due to the changes of the emission zone and the accompanying reduced Purcell effect. With increasing bias, the contribution of the Purcell effect monotonically increases, which leads to an increased decay time (see equation (4) below). The measured decay time in the inset to Fig. 7 reveals a bias region with increasing decay

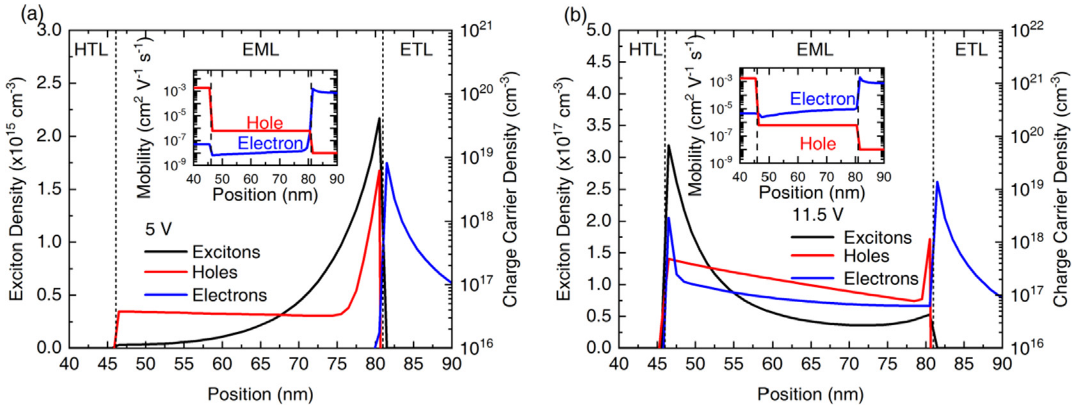

Fig. 5. Exciton distribution together with the hole and electron density profiles for 5 V (a) and 11.5 V (b). The insets show the effective hole and electron mobilities.

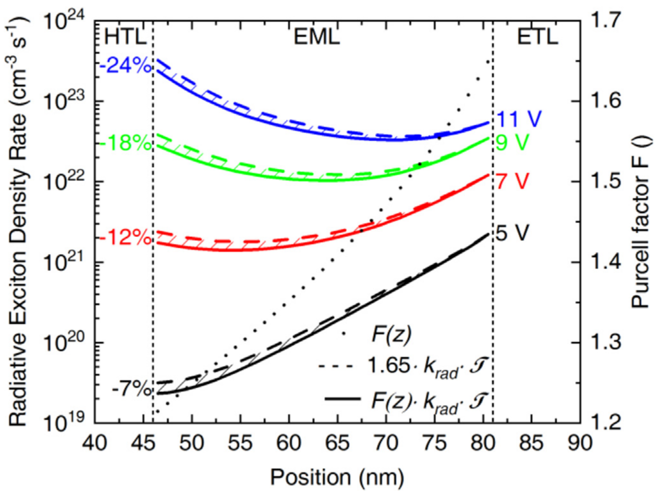

Fig. 6. Position-dependent Purcell factor F and calculated radiative exciton density rates with the true, position-dependent (solid lines) or fictitious, constant F of 1.65 (dashed lines).

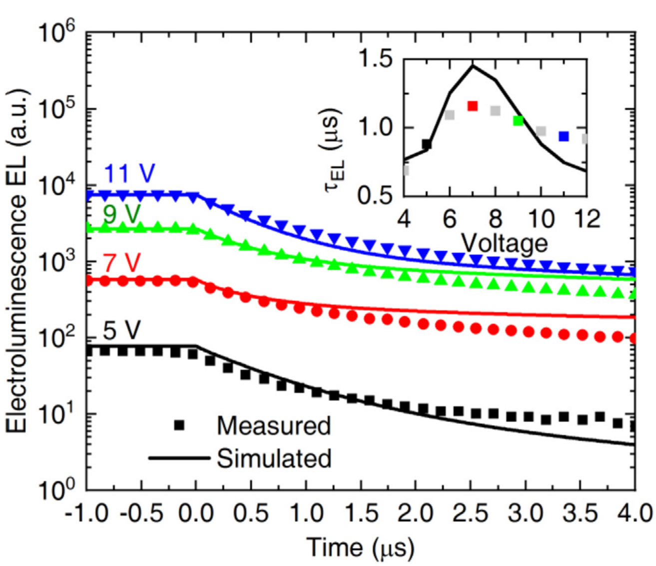

Fig. 7. Measured and simulated transient electroluminescence signals for different on-voltages. The inset shows the initial EL decay times extracted from the measured (symbols) and simulated (solid line) EL signal.

time, but also a bias region with decreasing decay time, thus the contributions from the Purcell effect alone cannot explain the measurements.

As discussed in the previous section, exciton quenching plays a dominant role in explaining the measured trend in current efficiency. Exciton quenching is also known to influence the radiative decay time τ in electroluminescence and in photoluminescence (PL) experiments. In the absence of exciton quenching, a mono-exponential decay of the PL signal is expected after the laser excitation is turned-off, because only the terms describing radiative and non-radiative decay remain in the exciton continuity equation (cf. equation (3)). In such a case, the PL decay time τ_{PL} is directly related to the (non-)radiative decay rates [34]

$$\tau_{PL} \propto \frac{1}{F\cdot k_{rad} + k_{nonrad}} \tag{4}$$

When the PL decay is measured while a bias is applied to the OLED, the electron and hole densities in equation (3) remain constant, thus allowing to elucidate the rates for TPQ with holes and electrons [28,34]. By varying the intensity of the exciting light, information about TTA can be obtained [41]. All PL experiments have in common that the exciton generation term vanishes immediately after the excitation source is switched off.

In contrast, the EL decay is fundamentally different, because the generation term in equation (3) can persist over long times, in our case a few microseconds. The generation term strongly depends on the applied bias before turn-off, and is influenced by a multitude of variables, foremost the charge carrier distribution, the electric field inside the EML and the charge carrier mobilities as discussed in the context of Fig. 8.

Fig. 7 shows the measured and simulated EL decay for different on-voltages. The simulation fits the measurements reasonably well, supporting the validity of the presented model. As a consequence of the significant contribution of the exciton generation and quenching terms, the EL decay is not mono-exponential anymore, and we find that the slope of the initial decay is not directly related to the (non-)radiative decay rates, especially after $t > 1\,\mu s$ and at high on-voltages. The inset to Fig. 7 shows the measured and simulated decay time τ_{EL} extracted from the initial slope of the EL decay ($t < 1\,\mu s$) assuming an exponential decay proportional to $\exp(-\frac{t}{\tau_{EL}})$.

To illustrate the complex interplay of the individual contributions in the exciton continuity equation (eq. (3)) on the EL decay, Fig. 8 shows the dominant terms integrated over the EML. At 5 V (Fig. 8a) the generation term ($\int G\cdot R\, dz$) decays over a long time because the effective charge carrier mobilities are low, which leads to a low Langevin recombination rate. Interestingly, at this bias, the generation term is essentially cancelled by the TPQ term for holes ($\int k_{TPQh}\cdot\mathscr{T}\cdot p\, dz$). The other terms are negligible, thus the EL decay is essentially mono-exponential even in the presence of high exciton quenching. In this special case where the generation term is essentially cancelled by the TPQh term, the radiative decay time τ_{EL} of 0.88 μs can be used to calculate the

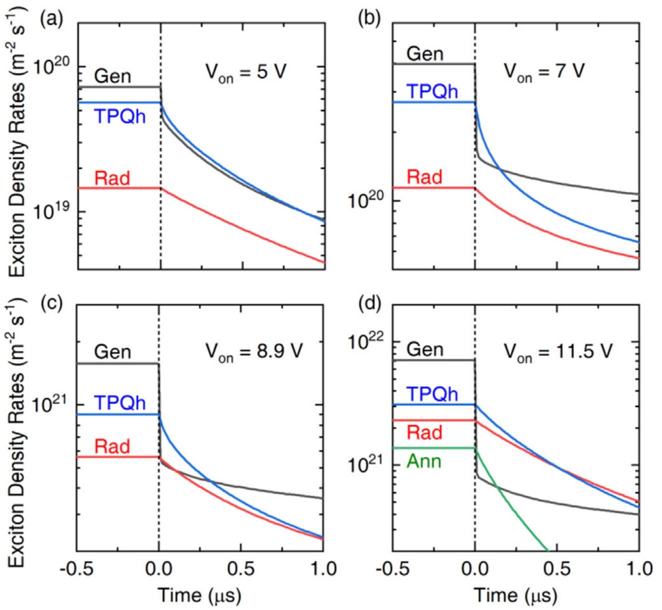

Fig. 8. Integrated exciton rates for generation (black lines), triplet-polaron quenching with holes (blue lines) and triplet-triplet annihilation (green line) to illustrate the respective contribution on the EL decay (red lines) at different biases.

intrinsic (non-)radiative decay rates from equation (4), if the intrinsic quantum efficiency ($q_0 = \frac{k_{rad}}{k_{rad} + k_{nonrad}} = 0.889$) and the Purcell factor are known. Using the Purcell factor where the exciton density at 5 V is largest ($F_{EML/ETL} = 1.65$), the values $k_{rad} = 0.64\ \mu s^{-1}$ and $k_{nonrad} = 0.08\ \mu s^{-1}$ were calculated, which agrees well with the values of $0.613\ \mu s^{-1}$ and $0.077\ \mu s^{-1}$ used in the simulations. With these rate constants, an intrinsic emitter lifetime of $\tau_{intrinsic} = \frac{1}{k_{rad} + k_{nonrad}} = 1.39\ \mu s$ was calculated, which is close to the value of $1.6\ \mu s$ measured in PL experiments in solution [42]. Thus, in the special case where certain terms in the exciton continuity equation cancel each other so that only the radiative and non-radiative terms remain, the mono-exponential EL decay can be used to extract the intrinsic emitter lifetime.

At intermediate biases (Fig. 8b and c), the generation term shows a sudden drop and the TQPh term is dominating the EL decay for $\approx 0.25\ \mu s$ before the generation term starts to dominate the decay. At high bias (Fig. 8d), the TTA term ($\int k_{ann} \cdot \mathscr{T}^2\, dz$) becomes significant up to $\approx 0.25\ \mu s$, after which it vanishes quickly. The generation term at this bias is also negligible and the EL decay is dominated only by TPQ with holes.

We like to note, that the individual contributions shown in Fig. 8 strongly depend on the OLED stack and, therefore, cannot easily be generalized. Nevertheless, Fig. 8 highlights that, in general, a full electro-optical model is required to extract the exciton rate constants and the intrinsic emitter lifetime from EL decay measurements.

4. Conclusion

We measured the current density - voltage - luminance (J-V-L), current efficiency (CE) and transient EL characteristics of a phosphorescent OLED. The current efficiency showed an unexpected increase up to 9 V followed by a decrease. An electro-optical model was devised to describe all measurements simultaneously. The model enabled insights into the mechanisms leading to the observed CE trends. A central outcome was that the emission zone changes with bias, which has manifold consequences. The bias-dependent emission zone causes an increase of the light outcoupling losses due to a reduced light outcoupling factor at high bias. Additionally, this shift of the emission zone significantly reduces the contribution of the triplet-polaron quenching at high bias, because the main emission occurs in a region with lower hole density. Only the combination of the reduced TPQ contribution with the increased light outcoupling losses and TTA contribution could explain the measured CE.

The model further allowed identifying individual contributions from the exciton continuity equation. Because of the dominating role of the exciton generation term, the EL decay is in general not mono-exponential, and the initial decay time is related to the intrinsic emitter lifetime only under special circumstances when the generation term is cancelled by the TPQ term.

This work highlights the benefits of an accurate knowledge of the emission zone and exciton quenching to reveal the details of the mechanism leading to the efficiency roll-off at high biases. An electro-optical model is, thus, a useful tool to identify strategies to further improve OLED efficiency.

Acknowledgements

We thank, S. Jenatsch, B. Blülle, S. Züfle, A. Stous and A. Gentsch from Fluxim AG and F. Nüesch from EPFL for fruitful discussions and valuable comments. Financial support from the Swiss National Science Foundation under grant no. 162230 is gratefully appreciated.

Appendix

Table 1
Optimized model parameters used in the electro-optical simulations.

	Optimized Parameters
PEDOT:PSS	
Work function (eV)	5.14
†Thickness (nm)	30
TCTA	
LUMO (eV)	2.3
HOMO (eV)	5.65
†,‡Mobility μ_e (m^2/Vs)	μ_0 = 3.3e-14, γ = 0.9e-3*
‡Mobility μ_h (m^2/Vs)	μ_0 = 1.8e-7, γ = 7.1e-7
†Thickness (nm)	46
CBP	
LUMO (eV)	2.56
HOMO (eV)	5.71
‡Mobility μ_e (m^2/Vs)	μ_0 = 3.1e-16, γ = 1.4e-3
‡Mobility μ_h (m^2/Vs)	μ_0 = 6.0e-11, γ = 4.5e-9
†Thickness (nm)	35
NBPhen	

Table 1 (*continued*)

	Optimized Parameters
LUMO (eV)	2.8
HOMO (eV)	6.4
‡Mobility μ_e (m^2/Vs)	μ_0 = 5.0e-8, γ = 1.5e-4
†,‡Mobility μ_h (m^2/Vs)	μ_0 = 1.0e-12, γ = 1.0e-8
†Thickness (nm)	52
Ca	
Work function (eV)	2.93
†Thickness (nm)	15
Excitonic Parameters in CBP	
Exciton formation ratio G (1)	1
Diffusion constant (nm^2/μs)	51.7
Radiative rate k_{rad} (μs^{-1})	0.61
Non-radiative rate k_{nonrad} (μs^{-1})	0.08
Annihilation rate k_{ann} (cm^3/s)	3.6e-12
TPQ e- rate k_{TPQe} (cm^3/s)	9.5e-14
TPQ h + rate k_{TPQh} (cm^3/s)	3.5e-12
†Dipole orientation (1)	0.24
Electric parameters	
†Series resistance R_s (Ohm)	10
†Parallel resistance R_p (MOhm)	15

† fixed model parameters.
‡ $\mu = \mu_0 \cdot e^{\gamma\sqrt{E}}$ with μ_0 zero field mobility, γ field coefficient and E electric field, *the large field-coefficient is a result of the optimization and could also be chosen much smaller without influencing the results.

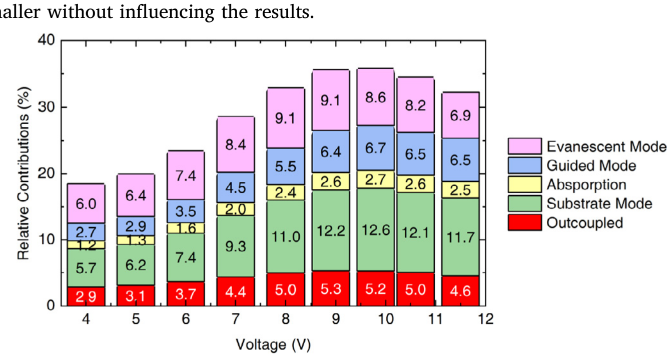

Fig. A1. Relative contributions of photons emitted into air and dissipated in the OLED stack where 100% corresponds to the total number of generated excitons (cf. Fig. 4).

References

[1] K.-H. Kim, S. Lee, C.-K. Moon, S.-Y. Kim, Y.-S. Park, J.-H. Lee, J. Woo Lee, J. Huh, Y. You, J.-J. Kim, Phosphorescent dye-based supramolecules for high-efficiency organic light-emitting diodes, Nat. Commun. 5 (2014) 4769, https://doi.org/10.1038/ncomms5769.
[2] K.-H. Kim, J.-L. Liao, S.W. Lee, B. Sim, C.-K. Moon, G.-H. Lee, H.J. Kim, Y. Chi, J.-J. Kim, Crystal organic light-emitting diodes with perfectly oriented non-doped Pt-based emitting layer, Adv. Mater. 28 (2016) 2526–2532, https://doi.org/10.1002/adma.201504451.
[3] K.-H. Kim, E.S. Ahn, J.-S. Huh, Y.-H. Kim, J.-J. Kim, Design of heteroleptic Ir complexes with horizontal emitting dipoles for highly efficient organic light-emitting diodes with an external quantum efficiency of 38%, Chem. Mater. 28 (2016) 7505–7510, https://doi.org/10.1021/acs.chemmater.6b03428.
[4] T.-H. Han, M.-R. Choi, C.-W. Jeon, Y.-H. Kim, S.-K. Kwon, T.-W. Lee, Ultrahigh-efficiency solution-processed simplified small-molecule organic light-emitting diodes using universal host materials, Sci. Adv. 2 (2016) e1601428, , https://doi.org/10.1126/sciadv.1601428.
[5] T.-A. Lin, T. Chatterjee, W.-L. Tsai, W.-K. Lee, M.-J. Wu, M. Jiao, K.-C. Pan, C.-L. Yi, C.-L. Chung, K.-T. Wong, C.-C. Wu, Sky-blue organic light emitting diode with 37% external quantum efficiency using thermally activated delayed fluorescence from spiroacridine-triazine hybrid, Adv. Mater. 28 (2016) 6976–6983, https://doi.org/10.1002/adma.201601675 Deerfield Beach Fla.
[6] C.-K. Moon, K. Suzuki, K. Shizu, C. Adachi, H. Kaji, J.-J. Kim, Combined inter- and intramolecular charge-transfer processes for highly efficient fluorescent organic light-emitting diodes with reduced triplet exciton quenching, Adv. Mater. 29 (2017) 1606448, https://doi.org/10.1002/adma.201606448.
[7] H. Kaji, H. Suzuki, T. Fukushima, K. Shizu, K. Suzuki, S. Kubo, T. Komino, H. Oiwa, F. Suzuki, A. Wakamiya, Y. Murata, C. Adachi, Purely organic electroluminescent material realizing 100% conversion from electricity to light, Nat. Commun. 6 (2015) 8476, https://doi.org/10.1038/ncomms9476.
[8] T. Komino, Y. Sagara, H. Tanaka, Y. Oki, N. Nakamura, H. Fujimoto, C. Adachi, Electroluminescence from completely horizontally oriented dye molecules, Appl. Phys. Lett. 108 (2016) 241106, https://doi.org/10.1063/1.4954163.
[9] J. Song, K.-H. Kim, E. Kim, C.-K. Moon, Y.-H. Kim, J.-J. Kim, S. Yoo, Lensfree OLEDs with over 50% external quantum efficiency via external scattering and horizontally oriented emitters, Nat. Commun. 9 (2018) 3207, https://doi.org/10.1038/s41467-018-05671-x.
[10] S. Jeon, J.-H. Lee, J.-H. Jeong, Y.S. Song, C.-K. Moon, J.-J. Kim, J.R. Youn, Vacuum nanohole array embedded phosphorescent organic light emitting diodes, Sci. Rep. 5 (2015) 8685, https://doi.org/10.1038/srep08685.
[11] J. Lee, T.-H. Han, M.-H. Park, D.Y. Jung, J. Seo, H.-K. Seo, H. Cho, E. Kim, J. Chung, S.-Y. Choi, T.-S. Kim, T.-W. Lee, S. Yoo, Synergetic electrode architecture for efficient graphene-based flexible organic light-emitting diodes, Nat. Commun. 7 (2016) 11791, https://doi.org/10.1038/ncomms11791.
[12] N.C. Giebink, B.W. D'Andrade, M.S. Weaver, P.B. Mackenzie, J.J. Brown, M.E. Thompson, S.R. Forrest, Intrinsic luminance loss in phosphorescent small-molecule organic light emitting devices due to bimolecular annihilation reactions, J. Appl. Phys. 103 (2008), https://doi.org/10.1063/1.2884530 044509.
[13] C. Murawski, K. Leo, M.C. Gather, Efficiency roll-off in organic light-emitting diodes, Adv. Mater. 25 (2013) 6801–6827, https://doi.org/10.1002/adma.201301603.
[14] S.R. Forrest, D.D.C. Bradley, M.E. Thompson, Measuring the efficiency of organic light-emitting devices, Adv. Mater. 15 (2003) 1043–1048, https://doi.org/10.1002/adma.200302151.
[15] B. Geffroy, P. le Roy, C. Prat, Organic light-emitting diode (OLED) technology: materials, devices and display technologies, Polym. Int. 55 (2006) 572–582, https://doi.org/10.1002/pi.1974.
[16] T. Tsutsui, N. Takada, Progress in emission efficiency of organic light-emitting diodes: basic understanding and its technical application, Jpn. J. Appl. Phys. 52 (2013) 110001, https://doi.org/10.7567/JJAP.52.110001.
[17] M. Regnat, K.P. Pernstich, S. Züfle, B. Ruhstaller, Analysis of the bias-dependent split emission zone in phosphorescent OLEDs, ACS Appl. Mater. Interfaces (2018),

https://doi.org/10.1021/acsami.8b09595.
[18] Paios, Platform for all-in-one Characterization of Solar Cells and OLEDs, Software Version Characterization Suit 4.12, Fluxim, Fluxim. (n.d.). https://www.fluxim.com/paios/.
[19] Setfos 5.0, Fluxim, Fluxim. (n.d.). https://www.fluxim.com/setfos-intro/.
[20] B. Perucco, N.A. Reinke, D. Rezzonico, E. Knapp, S. Harkema, B. Ruhstaller, On the exciton profile in OLEDs-seamless optical and electrical modeling, Org. Electron. 13 (2012) 1827–1835, https://doi.org/10.1016/j.orgel.2012.05.053.
[21] B. Ruhstaller, E. Knapp, B. Perucco, N. Reinke, D. Rezzonico, F. Müller, Advanced numerical simulation of organic light-emitting devices, in: Oleg Sergiyenko (Ed.), Optoelectron. Devices Prop. 2011 978-953-307-204-3 DOI 10577214626.
[22] B. Perucco, N.A. Reinke, F. Müller, D. Rezzonico, B. Ruhstaller, The influence of the optical environment on the shape of the emission profile and methods of its determination, Proc. SPIE (2010) 77220F1, https://doi.org/10.1117/12.853989.
[23] C. Adachi, M.A. Baldo, M.E. Thompson, S.R. Forrest, Nearly 100% internal phosphorescence efficiency in an organic light-emitting device, J. Appl. Phys. 90 (2001) 5048–5051, https://doi.org/10.1063/1.1409582.
[24] S. Naka, H. Okada, H. Onnagawa, T. Tsutsui, High electron mobility in bathophenanthroline, Appl. Phys. Lett. 76 (2000) 197–199, https://doi.org/10.1063/1.125701.
[25] S. Noh, C.K. Suman, Y. Hong, C. Lee, Carrier conduction mechanism for phosphorescent material doped organic semiconductor, J. Appl. Phys. 105 (2009), https://doi.org/10.1063/1.3072693 033709.
[26] S.-J. Yoo, H.-J. Yun, I. Kang, K. Thangaraju, S.-K. Kwon, Y.-H. Kim, A new electron transporting material for effective hole-blocking and improved charge balance in highly efficient phosphorescent organic light emitting diodes, J. Mater. Chem. C. 1 (2013) 2217–2223, https://doi.org/10.1039/C3TC00801K.
[27] S. Yamazaki, T. Tsutsui, Physics and Technology of Crystalline Oxide Semiconductor CAAC-IGZO: Application to Displays, John Wiley & Sons, 2017.
[28] S. Oyama, H. Sakai, H. Murata, Rate constant of exciton quenching of Ir(ppy) $_3$ with hole measured by time-resolved luminescence spectroscopy, Jpn. J. Appl. Phys. 55 (2016), https://doi.org/10.7567/JJAP.55.03DD13 03DD13.
[29] M.A. Parshin, J. Ollevier, M. Van der Auweraer, Charge carrier mobility in CBP films doped with Ir(ppy) 3, Proc. of SPIE, 2006, p. 61922A1, , https://doi.org/10.1117/12.663553.
[30] S.-B. Lee, T. Yasuda, M.-J. Yang, K. Fujita, T. Tsutsui, Charge carrier mobility in vacuum-sublimed dye films for light-emitting diodes studied by the time-of-flight technique, Mol. Cryst. Liq. Cryst. 405 (2003) 67–73, https://doi.org/10.1080/15421400390264162.
[31] H.-I. Baek, C. Lee, B.D. Chin, Comparison of the carrier mobility, unipolar conduction, and light emitting characteristics of phosphorescent host–dopant system, Synth. Met. 162 (2012) 2355–2360, https://doi.org/10.1016/j.synthmet.2012.11.008.
[32] M.T. Neukom, S. Züfle, B. Ruhstaller, Reliable extraction of organic solar cell parameters by combining steady-state and transient techniques, Org. Electron. 13 (2012) 2910–2916, https://doi.org/10.1016/j.orgel.2012.09.008.
[33] E. Knapp, B. Ruhstaller, Analysis of negative capacitance and self-heating in organic semiconductor devices, J. Appl. Phys. 117 (2015) 135501, https://doi.org/10.1063/1.4916981.
[34] S. Wehrmeister, L. Jäger, T. Wehlus, A.F. Rausch, T.C.G. Reusch, T.D. Schmidt, W. Brütting, Combined electrical and optical analysis of the efficiency roll-off in phosphorescent organic light-emitting diodes, Phys. Rev. Appl. 3 (2015), https://doi.org/10.1103/PhysRevApplied.3.024008 024008.
[35] N. Chopra, J. Lee, J. Xue, F. So, High-efficiency blue emitting phosphorescent OLEDs, IEEE Trans. Electron Devices 57 (2010) 101–107, https://doi.org/10.1109/TED.2009.2035028.
[36] W. Li, J. Li, F. Wang, Z. Gao, S. Zhang, Universal host materials for high-efficiency phosphorescent and delayed-fluorescence OLEDs, ACS Appl. Mater. Interfaces 7 (2015) 26206–26216, https://doi.org/10.1021/acsami.5b08291.
[37] C. Chen, C. Huang, J. Lee, C. Lin, T. Chiu, M. Leung, High efficiency blue phosphorescent organic light-emitting diode using tetraphenylsilane core molecule as host material, 2016 23rd Int. Workshop Act.-Matrix Flatpanel Disp. Devices AM-FPD, 2016, pp. 113–114, , https://doi.org/10.1109/AM-FPD.2016.7543636.
[38] Manual Setfos 4.6, Fluxim, n.d.
[39] P. Liehm, C. Murawski, M. Furno, B. Lüssem, K. Leo, M.C. Gather, Comparing the emissive dipole orientation of two similar phosphorescent green emitter molecules in highly efficient organic light-emitting diodes, Appl. Phys. Lett. 101 (2012) 253304, https://doi.org/10.1063/1.4773188.
[40] B. Sim, C.-K. Moon, K.-H. Kim, J.-J. Kim, Quantitative analysis of the efficiency of OLEDs, ACS Appl. Mater. Interfaces 8 (2016) 33010–33018, https://doi.org/10.1021/acsami.6b10297.
[41] M.A. Baldo, D.F. O'Brien, Y. You, A. Shoustikov, S. Sibley, M.E. Thompson, S.R. Forrest, Highly efficient phosphorescent emission from organic electroluminescent devices, Nature 395 (1998) 151–154, https://doi.org/10.1038/25954.
[42] S. Lamansky, P. Djurovich, D. Murphy, F. Abdel-Razzaq, R. Kwong, I. Tsyba, M. Bortz, B. Mui, R. Bau, M.E. Thompson, Synthesis and characterization of phosphorescent cyclometalated iridium complexes, Inorg. Chem. 40 (2001) 1704–1711, https://doi.org/10.1021/ic0008969.